# Comparative Study of Sub-THz FSS Filters Fabricated by Inkjet Printing, Microprecision Material Printing, and Photolithography

Oleksandr Sushko, Melusine Pigeon, Robert S. Donnan, Theo Kreouzis, Clive G. Parini, *Member, IEEE*, and Rostyslav Dubrovka, *Member, IEEE*

***Abstract*—This paper reports a comparative study of sub-THz frequency-selective surface (FSS) filter performance in relation to its method of fabrication. Three techniques are considered: conventional inkjet printing, microprecision inkjet printing, and photolithography. The complete design process is presented highlighting steps from substrate selection through to electromagnetic modeling and finally broadband THz filter characterization. Electromagnetic modeling is performed using the CST full-wave frequency-domain solver. Experimental characterization of substrate material, ink, and final FSS designs is done both by THz time-domain spectrometry and quasi-optically at WR-10 and WR-3 waveguide bands using PNA-X vector network analyzer. The center frequencies for bandpass FSS filters are 100 and 300 GHz, which enables prospective utilization in a quasi-optical multiplier system.**

***Index Terms*—Conductive ink, frequency-selective surface (FSS) filters, inkjet printing, quasi-optics, THz spectroscopy.**

## I. Introduction

WITH permanent technological advances over the last decade, componentry has matured significantly for sub-THz and THz frequency domain operation [1]. However, for both sources and detectors, THz components and circuitry remain costly. This has recently driven initiative to enhance existing techniques and to explore three-dimensional printing and conductive ink printing as an alternative method of fabrication [2], [3].

A proven, efficient, and long-standing method for near-lossless propagation and signal conditioning of THz radiation is by quasi-optical (QO) circuits [4]. Frequency-selective surfaces (FSS) are essential components for QO circuitry and serve various purposes, namely frequency-selective beam-splitting; filtering of higher order harmonics from a source; rejecting undesired signals and noise, etc. Two primary fabrication techniques for FSS filters are direct machining [5] and photolithography [6]. Photolithographic techniques, particularly, have been used to fabricate FSS filters for operation up to a few THz [7]. Advances in photolithography techniques and demand for low-loss THz signal conditioning have led to commercial availability of bandpass and lowpass FSS filters operating upto 20 THz [8]. The highest frequency of micromachined devices normally extends upto 0.5 THz [9]. Some techniques combine micromachining (with tolerances of $\pm 1$ $\mu$m), and wafer coating technologies to fabricate sub-THz FSSs [9]. Advanced micromachining in silicon, in combination with photolithography, allowed fabrication of a 0.7 THz FSS filter with $<$0.3 dB insertion loss [10]. Both techniques, however, are expensive (involving programmable microprecision machinery), and complex (requiring several stages of etching, development, coating, etc.). They mandate that high tolerances be met in fabricating an array composed of a unit cell having micron dimensions.

Conductive inkjet printing suggests a cost-effective alternative for fast prototyping of sub-THz FSS filters [11]–[15]. A comparison of sub-THz FSSs fabricated by traditional micromachining and those that are inkjet-printed is discussed by Walther *et al.* [11]. They report overall good agreement despite errors in center frequency values of up to 10%–15% due to inaccuracies in fabrication. The main drawback of this relatively new technique compared to others is poor resolution; however, this limitation is constantly diminishing [12]. Conductive-ink printing has been predominantly used for frequencies below 20 GHz. For example, Zabri *et al.* have discussed the realization of resistively loaded inkjet-printed FSS operations as a band-rejection filter at 15 GHz [13]. Inkjet conductive printing has proven feasible for antenna printing on textiles for wearable communications. A conventional dipole antenna operating at 2 GHz, inkjet-printed onto a fabric, has been demonstrated by Chauraya *et al.* [14]. Recently, inkjet conductive printing has been used for mm-wave applications. For instance, Oh *et al.* have demonstrated a rejection FSS filter for W-band based on a hexagonal unit cell [15]. Recent study by Sushko *et al*. investigated the angular dependence and origin of losses for bandpass FSS filters for 100 and 300 GHz, printed by a conventional ink-jet technique [16]. With advances including superfine inkjet printing, the structures produced can operate at around 1 THz. This opens up significant

Manuscript received September 15, 2016; revised December 6, 2016; accepted January 19, 2017. This work was supported by the Engineering and Physical Sciences Research Council, U.K., under Grant EP/K038125/1.

O. Sushko, M. Pigeon, R. S. Donnan, C. G. Parini, and R. Dubrovka are with the School of Electronic Engineering and Computer Science, Queen Mary University of London, London E1 4NS, U.K (e-mail: o.sushko@qmul.ac.uk; melusine.pigeon@gmail.com; r.donnan@qmul.ac.uk; c.g.parini@qmul.ac.uk; r.dubrovka@qmul.ac.uk).

T. Kreouzis is with the School of Physics and Astronomy, Queen Mary University of London, London E1 4NS, UK (e-mail: t.kreouzis@qmul.ac.uk).

Color versions of one or more of the figures in this paper are available online at http://ieeexplore.ieee.org.

Digital Object Identifier 10.1109/TTHZ.2017.2662582

possibilities to accelerate the development of THz and sub-THz QO components [12]. At present, however, superfine printing is costly.

This study focuses on the analysis of low-cost, sub-THz, FSS filters printed by conventional and microprecision inkjet printing and also compares these to those manufactured by photolithography.

## II. Materials and Methods

As a substrate for FSS filters, a *polyethylene terephthalate (PET) film* manufactured by Mitsubishi Paper Mills LTD is chosen (product NB-TP-3GU100). The thickness of the film is 135 $\mu$m and one side is coated by silver nanoparticle ink-accepting material ($\approx$1 $\mu$m thick), composed mainly of polyvinyl alcohol and aluminum oxide. This substrate has been used in all three fabrication methods.

Initial unit-cell dimensions were calculated using the *Modal Decomposition Equivalent Circuits Method* (MDECM), which is much faster than commercial solvers [17]. It is based on an aperture field theory; it models a periodic structure as an equivalent electrical circuit composed of admittances and ratio transformers. Further details can be found in [17].

The frequency-domain solver within the package of *CST Microwave Studio 14* is used to obtain the transmission response and finetuning of the periodic FSS filters. The periodic "unit-cell" boundary condition is applied on the plane of the array. The measured material properties of both the substrate and conductive layers serve as input to the solver to ensure a physically relevant prediction.

The design files to be utilized in printing and for the photolithography mask are prepared in *InkScape 0.48.4* software.

Three different techniques have been used to fabricate FSS filters. First, a *Brother* nanosilver inkjet printer *DCP 145C* (IJ) has been configured to print silver ink onto the coated paper and film materials**.** It is capable of providing up to 1200 $\times$ 6000 dpi resolution with a 4 picolitres (pL) minimum volume ink droplet. The ink selected for this printer is silver nano particle ink supplied by Mitsubishi Paper Mills LTD (product NBSIJ-MU01) whose main ingredients are silver (15%), ethylene glycol (15%–25%) and water (50%–70%).

Second, a *Dimatix Material Printer DMP-2831* has been exploited as an alternative to the Brother printer. The DMP is a bench-top flatbed materials' printer, designed for microprecision jetting of a variety of functional fluids, and conductive inks in particular. Key features of DMP are a tunable piezo inkjet cartridge, a 1 pL minimum volume droplet, and a feature-size of the order of 20 $\mu$m. Colloidal silver Ink—DryCureAG J for DMP printing has been purchased from Printed Electronics Ltd.

Finally, *photolithography* has been utilized as a mature methodology to pattern micron features of the FSS and is expected to be the most accurate among the three methods of patterning. All stages of photolithography were performed in a clean room. Special masks with the required patterns of filters to be used in a UV light-box are prepared prior to photolithography. At first, a PET substrate is covered by a 70 nm aluminum film using evaporation in a vacuum chamber. Coating thickness is controlled by the thickness-monitor located adjacent to the sample. A uniform photoresist (S1818) thin film is then applied atop the aluminum film by spin-coating at 6000 r/min. The sample obtained is cured at 90 °C for 15 min to allow evaporation of any remaining solvent from the photoresist. The sample is then treated by UV light through the mask for 1 min. Developing in a 1:3 sodium hydroxide–water solution for 90 s follows until a clear filter pattern forms. The final step is to wash away the remaining photoresist with acetone. According to our estimates, all the photolithographic processes involved in FSS fabrication had negligible effect on the mm-wave properties of the PET substrate.

The thickness of the printed films is measured by *a Dektak surface profilometer* operating a 12.5 $\mu$m stylus with 30–60 mN force.

Conventional *THz*-time-domain spectrometry (TDS) (transmission mode) serves to probe the broadband transmission response of the FSS filters and PET substrate. The core of the system is a 100 fs pulsed-laser, which excites a biased GaAs THz emitter. THz radiation is then focused onto the sample and subsequently transmitted to a ZnTe electro-optic detector by a train of four parabolic reflectors. The probe laser beam is delayed with respect to the pump beam by a mechanical delay stage. The voltage output of the balanced photodiode detector is proportional to the THz electric field amplitude, and is detected by a Stanford Lock-in Amplifier (SR850). The SNR of the THz-TDS system is estimated according to the guidelines suggested by Naftaly Dudley as a ratio between the mean peak amplitude and standard deviation of the peak [18]. The SNR of the system for frequency-domain spectra is $\sim$50 and is nearly constant across the 80 GHz to 2 THz spectral-band for the current setup.

For characterization of the substrate, measured at the THz beam focus of a THz-TDS, the *transfer function* used for estimating the complex dispersive refractive index is governed by [19]

$$\tilde{H}(f) = \tilde{t}_{12}(f)\,\tilde{t}_{21}(f)\exp\left(-i2\pi f d\left(\tilde{n}(f) - n_{\text{air}}\right)/c\right) \cdot \sum_{l=0}^{m}\left[\tilde{r}^2(f)\exp\left(-i4d\pi f\tilde{n}(f)/c\right)\right]^l \quad (1)$$

where $\tilde{n}(f) = n(f) - ik(f)$ is the complex refractive index of the sample, $d$ is the sample thickness; $\tilde{r}(f) = \frac{\tilde{n}(f)-n_{\text{air}}}{\tilde{n}(f)+n_{\text{air}}}$, $\tilde{t}_{12}(f) = \frac{2n_{\text{air}}}{\tilde{n}(f)+n_{\text{air}}}$, $\tilde{t}_{21}(f) = \frac{2\tilde{n}(f)}{\tilde{n}(f)+n_{\text{air}}}$ are the complex Fresnel coefficients at normal incidence; and *m* is the order of internal Fabry–Perot reflections. As seen from the transfer function (1), an account is taken of internal reflections of the THz signal within the sample. This provides a more accurate estimate of material parameters describing dispersive optical response. For characterization of the FSS filter, the ratio of its Fourier transform response to a "sample-free-path" background is used. Filters are also placed in the focused path of the THz beam for characterization. The diameter of the focusing mirrors is 50 mm and the focal distance is 100 mm, resulting is a solid angle of 28°.

*Network-analyzer-driven frequency-extension heads* operating at WR-10 (70–110 GHz) and WR-3 (220–325 GHz)

waveguide bands provide an additional means for characterization of the filters and materials involved. A pair of two such heads producing CW radiation enables acquisition of the full set of S-parameters for the sample under test. These heads are terminated with corrugated horns and, in combination with a set of reflectors (a two pairs of off-axis ellipsoids, coupling between an inner pair is faster to reduce the beam-waist in the focal plane), create a so-called "Z-bench" configuration for transmission measurements [5].

For extraction of material properties from PNA readings of transmission coefficient $S_{21}$, the *ABCD matrix* method is utilized [20]. For the case of a double-layered sample (i.e., conductive film on a substrate), the *ABCD* matrix is constructed for each layer and then multiplied to obtain the total *ABCD* matrix of the sample (2)

$$\begin{pmatrix} A & B \\ C & D \end{pmatrix}_{\text{total}} = \prod_{i=1}^{m} \begin{pmatrix} \cos(\beta l) & \mathrm{j}\cdot \mathrm{Z}\cdot \sin(\beta l) \\ \frac{\mathrm{j}\cdot\sin(\beta l)}{Z} & \cos(\beta l) \end{pmatrix}_i \tag{2}$$

where $Z = Z_0/\tilde{n}$ is the wave impedance of the material, $\beta = \omega\tilde{n}/c$ is a phase constant of propagation, $Z_0$ is the free space impedance, $l$ is the depth of the layer, and $m$ is the total number of layers (two in our case).

Then, $S_{21}$ transmission function is determined based on *ABCD* values as follows:

$$S_{21} = \frac{2Z_0}{AZ_0 + B + CZ_0^2 + DZ_0}. \tag{3}$$

The undetermined coefficients of interest (i.e., the material properties) are then obtained by minimizing the error between the transmission function and the experimental readings. Conductivity is obtained from the dielectric response with the assumption that the material under test is a good conductor, i.e.

$$\sigma = i\varepsilon_0\varepsilon''\omega.$$

Note that printing multiple layers of conductive ink (which are known to improve conductivity [21]), was not used in this study. Advances in material science also removed the need for sintering for most of the commercially available conductive inks and paints [21].

## III. Results and Discussion

Two approaches are possible for the intended comparative analysis: 1) to optimize and fabricate all filters for the same center-frequency and analyze differences in unit-cell dimensions for each fabrication method or 2) to fabricate filters using the same design for each technique and investigate differences in their response (center frequencies and insertion losses in particular). In this study, the second approach is chosen due to its faster implementation. The first step is to determine material properties of the PET substrate in the frequency bands of interest. Fig. 1 shows the real and imaginary parts of the complex dielectric constant extracted by THz-TDS. The dielectric properties are 3.015 – i0.047 and 2.998 – i0.059 at 100 and 300 GHz, respectively, which agrees with the previously published data for PET material [22]. Accurate properties of the conductive layers also have to be known for reliable modeling of filter response,

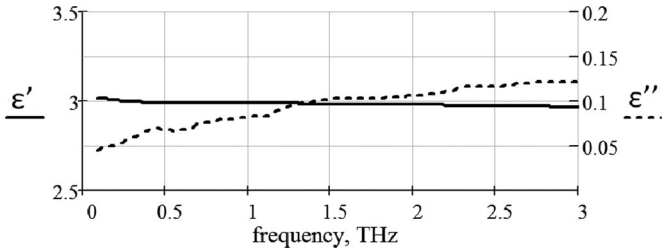


Fig. 1. Real (solid) and imaginary (dashed) parts of the complex dielectric constant of polyethylene terephthalate (PET) substrate.

TABLE I
Conductivity in MS/m of Materials Used at 100 and 300 GHz Derived From Analysis of Data Read From a Vector Network Analyzer Driving a Quasi-Optical Analysis Circuit

| Filter band, GHz | IJ, MS/m | DM, MS/m | PL, MS/m |
|---|---|---|---|
| 100 | 0.29 | 3.3 | 21 |
| 300 | 0.08 | 1.8 | 20 |

since conductivity of different inks varies in particular. For pure aluminum, the conductivity is a few times lower in the sub-THz band than at dc values [23]. Table I provides details of the estimated conductivity values of the printed surface for the three investigated techniques of Inkjet Brother Printer (IJ), Dimatix Material Printer (DM), and photolithography (PL). The lowest conductivity of $0.8 \times 10^5$ S/m is found to be that for the silver nanoparticle ink used for inkjet printing at 300 GHz, while the aluminum film, as expected, has the highest conductivity among the three.

The conductivity of metals normally drops at higher sub-THz frequencies as described by the Drude model. The same effect can be observed for IJ and DM inks where conductivity at 100 GHz is higher than at 300 GHz.

The first technique used in this study to fabricate the FSS filters was IJ printing, consequently dimensions of unit cells were optimized considering the respective resolution of the IJ print. Therefore, the slot-geometry is rectangular for the 100 GHz bandpass filter and square for the 300 GHz filter. Despite the FSS based on square-slots being less selective, they provide lower loss; rectangular slots were not feasible for a 300 GHz bandpass filter fabricated by IJ printing. For the other techniques (DM and PL), designs are kept the same for the purpose of comparison. To get an initial design of the unit cell and slot-sizes, a fast home-built MDECM analysis tool is used [17]. It was shown to provide fast (one run taking a fraction of a second) and reasonably accurate frequency-response analysis of periodic surfaces on dielectric substrates. Its results are compared later in the text with CST modeling and measurements. The initial unit-cell dimensions, together with material properties of the PET substrate and conductive layers, are then fed into CST for simulations. The respective thickness of each conductive layer (0.5 $\mu$m for inkjet printer, 1 $\mu$m for Dimatix printer, and 70 nm for photolithography), is also considered in the CST model. The resulting FSS geometry used for fabrication by the

TABLE II
PICTORIAL SUMMARY OF THE GEOMETRIC QUALITY OF APERTURES PREPARED BY THE THREE PATTERNING METHODOLOGIES

| Fabrication method | 100 GHz FSS filter, 1.4 x 1.0 mm$^2$ cell 1.07 x 0.30 mm$^2$ slot | 300 GHz FSS filter, 0.5 x 0.5 mm$^2$ cell 0.28 x 0.28 mm$^2$ slot |
|---|---|---|
| *Inkjet printed* | 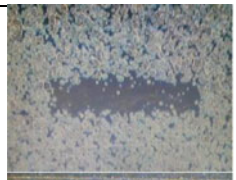 |  |
| *Dimatix MP* |  | 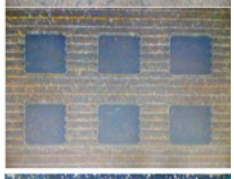 |
| *Photo-lithography* | 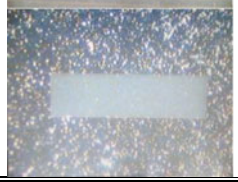 | 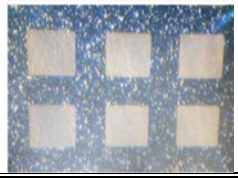 |

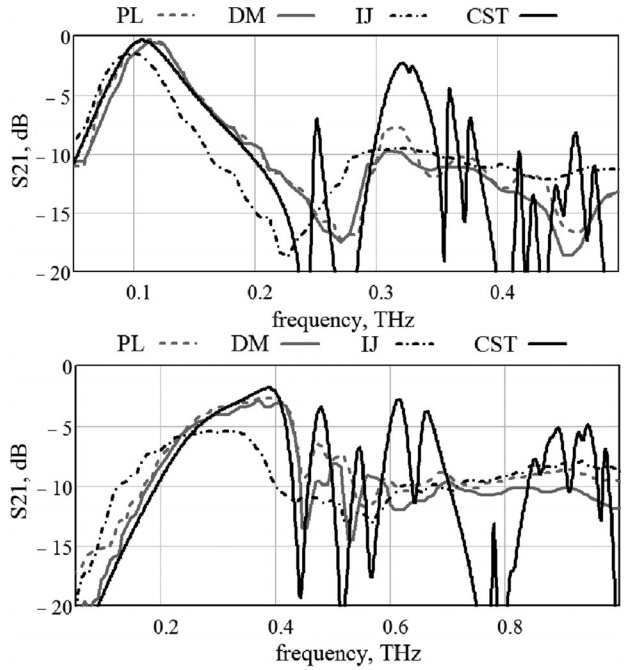


Fig. 2. Measured and simulated transmission properties of the FSS filters: 100 GHz bandpass filter (upper plot) and 300 GHz bandpass filter (lower plot). CST simulations correspond to the DM-printed FSS filter. Measured plots have ±2% noise-dictated uncertainty at the peak transmission.

three different techniques is a 1.07 × 0.30 mm$^2$ slot within a 1.4 × 1.0 mm$^2$ unit cell for the 100 GHz bandpass filter and, 0.28 × 0.28 mm$^2$ slots within a 0.5 × 0.5 mm$^2$ unit cell for the 300 GHz filter. Considering the beam waist of THz radiation at the focal point (4 mm at 100 GHz and 2 mm at 300 GHz), and the feature size of the filters, approximately 27 unit cells are illuminated for a 100 GHz filter and 35 for a 300 GHz bandpass filter.

Microscope images of the FSS filters fabricated by these different techniques are shown in Table II. Note that ink dots visible on the image for IJ-printed FSSs are not a separate nanoparticle, but groups of thousands of such, as the size of individual silver nanoparticle is of the order of 20 nm. Only one and six cells are shown for 100 and 300 GHz filters, respectively. However, the actual filters that were fabricated consist of 25 × 35 and 64 × 64 slot apertures, corresponding respectively to the 100 and 300 GHz FFS filters. IJ fabrication exhibits the lowest resolution and highest porosity of the ink among the three. The dimensions of the slots for the 300 GHz filter are close to the resolution limit of the IJ printer, therefore slot-edges are poorly defined. If directly converted, the IJ printer resolution (max. 1200 × 6000 dpi) corresponds to a dot-spacing of 21 × 4.2 $\mu$m, which is clearly not the case. However, the achieved resolution of conventional IJ-printing, with conductive inks, is typically lower than the stated maximum value for a given printer [13], [21]. The reason for the poorer quality of conductive printing might originate from the specific interaction of ink composition/structure with jetting-nozzles. In addition, we have not used disposable filters [21] to remove any contaminants or clogging particles which could have an impact on our printed structures. DM printing is performed in 70 –75 $\mu$m wide conductor lines. The features of the slots are sharp, except for the small ridges of about 5–10 $\mu$m high at the sides of the slot and rounding at corners with a radius of curvature of 20–30 $\mu$m. FSSs fabricated by PL yield well-defined straight edges with an approximate 10–15 $\mu$m radius-of-curvature corners.

TABLE III
MEASURED SLOT DIMENSIONS FOR THE FABRICATED FILTERS

| Fabrication method | Slot dimensions for 100 GHz FSS filter, $\mu$m (nominal: 1070 × 300 $\mu$m) | Slot dimensions for 300 GHz FSS filter, $\mu$m (nominal: 280 × 280 $\mu$m) |
|---|---|---|
| Inkjet printed | 1034 (15) × 276 (13) | 261 (11) × 253 (10) |
| Dimatix MP | 1050 (9) × 289 (7) | 280 (8) × 277 (7) |
| Photolithography | 1069 (3) × 300 (3) | 278 (2) × 276 (3) |

Values in Brackets Show One Standard Deviation of the Estimation.

White dots on the images of PL filters are due to reflection of light from metalized microbumps on the PET sheet. All filters are made on the same 135 $\mu$m thick PET substrate; the difference in substrate colors in the images originates from automatic illumination-adjustment of the camera. Simulated filter transmission response by CST and that measured by THz-TDS, are depicted in Fig. 2. The actual slot-dimensions of the fabricated filters are measured by a microscope (EVOCam from Vision Engineering Ltd) via fitting a rectangle into the slot. Table III shows the measured sizes of slots for each filter with a respective confidence interval, taken as one standard deviation of ten measurements.

For DM and PL filters, the measurement of the slot-size is more deterministic due to sharper edges. For the IJ FSS, the slot geometry cannot be precisely characterized, which is also confirmed by higher deviations in Table III. Slots of the IJ-print are typically undersized by several percent. As expected, PL-fabricated filters on the other hand most accurately corre-

TABLE IV
COMPARISON OF CENTER FREQUENCIES AND LOSSES FOR THE INVESTIGATED FABRICATION TECHNIQUES

| | | IJ | | DM | | PL | |
|---|---|---|---|---|---|---|---|
| | | Simul. | Meas. | Simul. | Meas. | Simul. | Meas. |
| 100 GHz | $f_0$, GHz | 105.4 | 103 (1) | 106.3 | 116 (1) | 105.8 | 113 (1) |
| | Losses at $f_0$, dB | 0.62 | 1.35 (0.03) | 0.4 | 0.50 (0.01) | 0.34 | 0.43 (0.01) |
| 300 GHz | $f_0$, GHz | 378.7 | 285 (1) | 385.9 | 370 (1) | 387.2 | 384 (1) |
| | Losses at $f_0$, dB | 2.4 | 5.40 (0.11) | 1.90 | 3.0 (0.06) | 1.7 | 2.7 (0.05) |

spond to nominal dimensions and have lowest deviations. In regard to deviation, the DM-fabricated 300 GHz FSS falls within the nominal size, while the 100 GHz filter is slightly undersized.

The bold, black, curve in both plots represents the simulated results for DM-prepared filters. Simulated properties for IJ and PL filters are not shown as they closely resemble that for the DM type, especially at 100 GHz. More details on the losses and center-frequency performance of the FSS filters made by the three different techniques are given in Table IV. The noise-driven uncertainty of the measured losses in Table IV is $\pm 2\%$. Absolute uncertainty values for the measured results in Table IV are shown in brackets. It is seen that due to some differences in simulated and measured center frequencies, rescaling of filter geometry may be required to obtain the desired filter performance. Center frequency $f_0$ is considered the frequency where filters have maximum $S_{21}$ transmission.

All the simulated values in Table IV are given for nominal dimensions of filters. Concerning the measured dimensions provided in Table III, the match with measurements is improved for the 100 GHz DM filter to 0.43 dB losses for a center frequency at 107.6 GHz. On the other hand, the agreement between the simulated and measured results degrades in terms of center frequency, but improves in terms of losses for IJ filters when taking into account measured slots-size, i.e., 0.68 dB at 107.67 GHz and 2.83 dB at 374 GHz.

Despite the center frequency of the IJ FSS at 100 GHz is closer to simulations, the overall shape of the simulated $S_{21}$ response is better reproduced by DM and PL filters (see Fig. 2). The sharp peaks above the design frequency in the simulated transmission spectra are dictated by the higher order modes. On the other hand, measurement results are flatter for the reason that these modes are more dampened in real FSS filters than in simulations. Also the mismatch is due to the fact that the dielectric constant of PET and its conductivity are only valid for the design frequency in simulations. However, some high frequency features above center frequency were reproduced by DM and PL FSSs, but not for IJ filters. These include, for instance, a transmission peak at 320 GHz for the 100 GHz bandpass filters and $S_{21}$ ripples in the 400–600 GHz spectral domain for the 300 GHz filters. The general trend also is still preserved. For instance, at the higher frequency end of the plots shown, the simulated plots fluctuate closely around the measured curves. The variations between models of filters were the conductivity and the thickness of metallization, while the quality of the features was not taken into account. These two parameters are critical for accurate prediction of FSS performance. Resonant frequency is proportional to both parameters; losses, on the other hand, are reduced for larger conductivity values and lower thickness of the FSS material. Importantly, there is a knee-value (above a 1–2 $\mu$m thickness and below $\sigma = 10^4$ S/m), in both dependences after which losses and resonant frequency are affected more strongly. For instance, a lower conductivity by one order of magnitude can result in a noticeable red-shift in $S_{21}$ together with a jump in loss (for instance, according to simulations, for $\sigma = 10^4$ S/m: $f_0 = 102.4$ GHz and losses are 1.6 dB). Table IV illustrates that the measured performance of the filters generally agrees in trends with simulations. Interestingly, the measured DM filter center frequency is higher than the more conductive PL filter at 100 GHz, which is due to the larger thickness of the conductive layer that overtakes the conductivity difference. As expected, the most noticeable discrepancy between measured and simulated losses is observed for IJ FSS due to the quality of printed filter features. Also, the difference between the predicted and measured losses is higher for the 300 GHz filter, since any fabrication defects are larger in terms of operating wavelength. The higher insertion losses of the IJ filter are attributed, besides lower conductivity, to the porous ink distribution, as can be seen from the irregular slot-edges and some undesired ink dots present within the apertures. A reason for discrepancy between simulations may be the fact that the thin ($\sim$1 $\mu$m) ink-accepting layer on top of the PET sheet is ignored, so that during characterization, the PET substrate is considered uniform. Another source of error is that a dispersive conductivity is not considered in simulations, instead a single frequency value was used. The same concerns the material properties of substrate, i.e., the center-frequency values are provided and the CST solver then extrapolates to span the band. Possible variations in the thickness of either the conductive layer or the PET substrate could also contribute to the disparity. Although, in general, the agreement between simulations and measurements is rather good, the best match is achieved when the measured values of conductivity are lowered, primarily in the case of IJ, but also for DM and PL filters. Such a difference cannot be entirely explained by the conductivity dispersion and the ignored ink-accepting layer. The major contribution to this disparity is the porous ink distribution for the case of IJ filters and the uneven surface for the case of DM filters, resulting in a less precise definition of effective medium parameters of ink.

The three main sources of loss, namely dielectric substrate loss, conduction loss, and fabrication imperfections, contribute variously as expected, depending on the fabrication technique and the frequency of operation. The former two are investigated numerically using CST. For the IJ filter at 100 GHz, the conduction losses contribute about 32% of total losses (0.19 out of 0.62 dB). On the other hand, at 300 GHz, total losses are more dominated by the substrate contribution and only 24% is attributed to conduction loss (0.48 out of 2.4 dB). The difference between the simulated and measured losses, 0.73 dB at 100 GHz and 3.0 dB at 300 GHz, is attributed mainly to printing imperfections of the unit cell in the IJ FSS. Clearly, at higher frequencies, dielectric losses prevail over all others. Losses in

DM and PL FSS filters are dominated even more by the substrate, since conductivity is higher than in IJ filters. For instance, at 300 GHz for DM and PL filters, only 0.13 dB and 0.05 dB out of total 1.9 and 1.6 dB are due to conduction losses. This accentuates the importance of using thin and low-loss substrates (or ideally free-standing/self-supporting structures), for designing FSS filters for sub-THz frequencies.

Based on the above analysis, structures made by the IJ fabrication technique have the smallest feature resolution of about 200–300 $\mu$m. This limits its highest operational frequency to approximately 200 GHz. Photolithography on the other hand possesses comparatively higher resolution and has been used elsewhere to produce FSS filters, even for the mid-infrared wave band [7]. However, it involves several tedious steps including preparation of the mask, spin-coating, chemical developing, etc., making it a comparatively complex, time-consuming and costly route for a nonserial fabrication line. Microprecision printing by a Dimatix material printer offers a compromise in terms of THz performance and practicability of fabrication. Considering the resolution of printing and conductivity of inks, the DM FSS filters are projected to operate without excessive losses up to 1 –1.5 THz. This frequency limit imposes that thin and low-loss substrates be used.

## IV. Conclusion

FSS bandpass filters operating at 100 and 300 GHz have been fabricated by conventional (IJ) and microprecision (DM) inkjet printing and photolithography. Numerical modeling in CST MWS is used to optimize the design of the FSS devices. The wideband transmission properties are studied by THz-TDS. Simulated and experimental results agree well with average deviation in center-frequency of about 5%–10%. It is shown that scaling filters to higher THz frequencies requires low-loss and thinner substrates, since substrate losses become dominant above 100 GHz. Alternative materials with lower dielectric constant can move the usable frequency limit higher by enlarging the equivalent size of the array elements. For improving selectivity and rejection performance, other more complex unit-cell elements can be studied. The Dimatix printer is equipped with the possibility of precisely applying multiple layers of ink, which increases the conductivity and thickness and, in turn, selectivity is thereby enhanced. Dimatix printing offers fast and easy fabrication of FSS structures together with workably high ink-conductivity and resolution leading to cut-off frequencies of FSS filters of up to 1.5 THz.

## References


[1] A. Redo-Sanchez, N. Laman, B. Schulkin, and T. Tongue, "Review of terahertz technology readiness assessment and applications," *J. Infrared Millim. THz Waves*, vol. 34, no. 9, pp. 500–518, 2013.

[2] S. Pandey, B. Gupta, and A. Nahata, "Terahertz plasmonic waveguides created via 3D printing," *Opt. Exp.*, vol. 21, no. 21, pp. 24422–24430, 2013.

[3] B. S-Y. Ung, B. Weng, R. L. Shepherd, D. Abbott, and C. Fumeaux, "Inkjet printed conductive polymer-based beam-splitters for terahertz applications," *Opt. Mater. Exp.*, vol. 3, no. 9, pp. 1242–1249, 2013.

[4] P. F. Goldsmith, *Quasioptical Systems: Gaussian Beam Quasoptical Propagation and Applications*. Hoboken, NJ, USA: Wiley, 1998.

[5] Y. Wang, B. Yang, Y. Tian, R. S. Donnan, and M. J. Lancaster "Micromachined thick Mesh filters for millimeter-wave and terahertz applications," *IEEE Trans. THz Sci. Technol.*, vol. 4, no. 2, pp. 247–253, Mar. 2014.

[6] M. E. MacDonald, A. Alexanian, R. A. York, Z. Popovic, and E. N. Grossman, "Spectral transmittance of lossy printed resonant-grid terahertz bandpass filters," *IEEE Trans. Microw. Theory Techn.*, vol. 48, no. 4, pp. 712–718, Apr. 2000.

[7] S. A. Kuznetsov *et al.*, "FSS-filters and metasurfaces for subterahertz and terahertz frequencies," in *Proc. 3rd Int. Congr. Adv. Electromagn. Mater. Microw. Opt.*, 2009, pp. 391–393.

[8] A. M. Melo, A. L. Gobbi, M. H. O. Piazzetta, and A. M. P. A. da Silva, "Cross-shaped terahertz metal mesh filters: Historical review and results," *Adv. Opt. Technol.*, vol. 2012, 2012, Art. no. 530512.

[9] B. G. Xia *et al.*, "Terahertz FSS for space borne passive remote sensing application," *Electron. Lett.*, vol. 49, no. 22, pp. 1398–1399, Oct. 2013.

[10] R. Dickie, R. Cahill, V. Fusco, H. S. Gamble, and N. Mitchell, "THz frequency selective surface filters for earth observation remote sensing instruments," *IEEE Trans. Terahertz Sci. Tech.*, vol. 1, no. 2, pp. 450–461, Nov. 2011.

[11] M. Walther *et al.*, "Terahertz metamaterials fabricated by inkjet printing," *Appl. Phys. Lett.*, vol. 95, 2009, Art. no. 251107.

[12] K. Takano *et al.*, "Fabrication of terahertz planar metamaterials using a super-fine ink-jet printer," *Appl. Phys. Exp.*, vol. 3, 2010, Art. no. 016701.

[13] S. N. Zabri, R. Cahill, G. Conway, and A. Schuchinsky, "Inkjet printing of resistively loaded FSS for microwave absorbers," *Electron. Lett.*, vol. 51, no. 13, pp. 999–1001, 2015.

[14] A. Chauraya *et al.*, "Inkjet printed dipole antennas on textiles for wearable communications," *IET Microw. Antennas Propag.*, vol. 7, no. 9, pp. 760–767, 2013.

[15] J. Oh, S. Cho, C. Lee, J. Kim, and B. Choi, "The fabrication of film-type frequency selective surface (FSS) attachable to window glass using inkjet printing technique," in *Proc. 2008 URSI Gen. Assembly Sci. Symp.*, Chicago, IL, USA, Aug. 2008.

[16] O. Sushko *et al.*, "Low-cost inkjet-printed FSS band-pass filters for 100 and 300 GHz," in *Proc. 10th Eur. Conf. Antennas Propag.*, Davos, Switzerland, Apr. 2016, pp. 1–3.

[17] R. Dubrovka, J. Vasquez, C. Parini, and D. Moore, "Equivalent circuit method for analysis and synthesis of frequency selective surfaces," *Proc. IEE—Microw. Antennas Propag.*, vol. 153, no. 3, pp. 213–220, Jun. 2006.

[18] M. Naftaly and R. Dudley, "Methodologies for determining the dynamic ranges and signal-to-noise ratios of terahertz time-domain spectrometers," *Opt. Lett.*, vol. 34, no. 8, pp. 1213–1215, 2009.

[19] O. Sushko, K. Shala, R. Dubrovka, and R. Donnan, "Revised metrology for enhanced accuracy in complex optical constant determination by THz-time-domain spectrometry," *J. Opt. Soc. Amer. A, Opt. Image Sci.*, vol. 30, no. 5, pp. 979–986, 2013.

[20] B. Yang, K. Shala, X. Liu, H. Su, and R. S. Donnan, "Complex permittivity of pure water measured by vector network analysis at W-Band," *J. Phys. Conf. Ser.*, vol. 286, 2011, Art. no. 012005.

[21] Y. Kawahara, S. Hodges, B. S. Cook, C. Zhang, and G. D. Abowd "Instant inkjet circuits: Lab-based inkjet printing to support rapid prototyping of UbiComp devices," in *Proc. ACM Int. Joint Conf. Pervasive Ubiquitous Comput.*, Zurich, Switzerland, Sep. 2013, pp. 363–372.

[22] Y.-S. Jin, G.-J. Kim, and S.-G. Jeon, "Terahertz dielectric properties of polymers," *J. Korean Phys. Soc.*, vol. 49, no. 2, pp. 513–517, 2006.

[23] M. P. Kirley and J. H. Booske, "Terahertz conductivity of copper surfaces," *IEEE Trans. THz Sci. Technol.*, vol. 5, no. 6, pp. 1012–1020, Nov. 2015.



**Oleksandr Sushko** M.Sc. (Hons.) degree in radio-engineering from the National Technical University of Ukraine "Kyiv Polytechnic Institute," Kyiv, Ukraine, in 2010, and the Ph.D. degree from the Antennas and Electromagnetics Group, Queen Mary University of London, London, U.K., in 2014. His disseration was entitled "Terahertz dielectric study of bio-molecules using time-domain spectrometry and molecular dynamics simulations."

He then continued working with the Antennas and Electromagnetics Group as a Postdoctoral Research Assistant, first on development of mm-wave components for a new generation of space-born sounder for meteorological satellites, then on the development of quasi-optical sub-THz sources-based arrays of Schottky diodes. His research interests include THz materials characterization and liquid spectroscopy, mm-wave and THz antennas and components, and quasi-optical circuits and their applications.

**Melusine Pigeon** received the M.Sc. degree in engineering from the National School of Civil Aviation (ENAC), Toulouse, France, in 2007, and the Ph.D. degree in microwave, electromagnetism, and optoelectronics from the Institut National Polytechnique (INP) de Toulouse, Toulouse, in 2011.

After holding different postdoctoral positions with the CEA-LETI, Grenoble, France, and at the Institut d'électronique et de télécommunications de Rennes (IETR), Rennes, France, she now holds a Postdoctoral Fellowship with Queen Mary University of London, London, U.K. Her research interests include antennas at terahertz frequencies, compact antennas, metamaterials, and antenna fundamental limitations.

**Robert S. Donnan** received the B.Sc. degree in mathematical physics from the University of Wollongong, NSW, Australia, in 1990, the M.Sc. degree in applied physics from the University of Technology, Sydney, in 1995, and the Ph.D. degree in solid state physics from the University of Wollongong, in 2000.

In 2001, he joined the Queen Mary University of London as a Research Assistant with the Antennas and Group, Department of Electronic Engineering. He was appointed as a Lecturer in 2003, promoted to Senior Lecturer in 2013, and to a Reader in terahertz engineering in 2015. He founded the Terahertz Metrology Laboratory within the School of Electronic Engineering and Computer Science in 2009, which develops and applies methods of antenna metrology to the life sciences broadly and to basic and applied research in millimetre-wave and THz engineering specifically.

Dr. Donnan is a Fellow of the Institute of Physics, a Fellow of the IET, a Chartered Physicist and general committee member of the Instrument Science and Technology Group, U.K. Institute of Physics.

**Theo Kreouzis** received the Ph.D. degree in physics in 1999 for his work on transient photoconduction measurements on discotic liquid crystals.

He spent four years as a Postdoctoral Researcher with Queen Mary and Imperial College, measuring charge transport in various organic systems, before being appointed as a Lecturer with the Department of Physics, Queen Mary College, University of London, in 2003. Since taking up post he has researched charge transport on reactive mesogens, polymer and small molecule organic semiconductors using transient (photo) conduction techniques and has supervised approximately 8 Ph.D. students to date. As of 2015, he has authored or co-authored more than 60 papers in peer-reviewed journals, has an h-index of 22, and was currently promoted to a Senior Lecturer. For the past ten years, he has been researching the effects of excited states and magnetic fields on charge transport in organic semiconductors with a view to elucidate the microscopic mechanisms behind organic magnetoresistance. He has worked on the effect of photogenerated charges and excited states on the dielectric properties of conjugated polymers. Most recently, he has also begun research on radiation detection using organic semiconductors.

**Clive G. Parini** (M'96) received the B.Sc.(Eng) and Ph.D. degrees from Queen Mary University of London, London, U.K., in 1973 and 1976 respectively.

He joined Queen Mary University of London, London, U.K., as a Lecturer in 1977, was promoted to a Reader in 1990, then a Professor in 1999, and is currently a Professor of antenna engineering and heads the Antenna and Electromagnetics Research Group. He has authored or co-authored more than 450 papers on research topics, including array mutual coupling, array beam forming, antenna metrology, microstrip antennas, millimeter-wave compact antenna test ranges, millimeter-wave integrated antennas, metamaterials, and on-body communications. In 2007, he co-authored *Principles of Planar Near-Field Antenna Measurements* (IET, Electromagnetic Wave Series), and in 2014 the book entitled *Theory and Practice of Modern Antenna Range Measurements* (IET, Electromagnetic Wave Series).

Dr. Parini is a Fellow of the IET, a past Chairman of the IET Antennas & Propagation Professional Network Executive Team and a Chartered Engineer. He was a member of the Editorial Board until January 2015 and past Honorary Editor for the *IET Journal Microwaves, Antennas & Propagation*. In 2009, he was elected a Fellow of the Royal Academy of Engineering.

**Rostyslav Dubrovka** (M'04) received the M.Sc., MBA, and Ph.D. degrees from the National Technical University of Ukraine "Kyiv Polytechnic Institute," Kyiv, Ukraine, in 1993, 1997, and 2000, respectively.

In 1997, he became an Executive Manager of a small research and development company in Kyiv, continuing his research activity. He joined the Antenna and Electromagnetics Group, Queen Mary University of London, in February 2001, as a Postdoctoral Research Assistant. In 2006, he became an Antenna CAD/CAM Engineer, and in 2014, a Terahertz and Quasi-Optics Research Lab Manager. From 1991 to 2000, his research covered the areas of mm-wave slot antenna arrays, microwave planar devices, including optically controlled active elements, finite aperture antenna arrays, and feed systems for various reflector systems of various size and configurations, including 5 and 7 m hub stations, VSAT antennas, radio-relay reflector antennas, etc. Since 2001, his research has covered compact corrugated horns, new equivalent circuit method for design of frequency-selective surfaces, methods of analysis for on-body propagation, low-mass low-profile antenna arrays for air-born synthetic aperture radars, modeling techniques and applications of metamaterials for mm-wave quasi-optical earth observation radiometers, wire media applications for antennas, design of quasi-optical networks for a new generation of space-born sounders for meteorological satellites, and THz spectroscopy for life sciences. He is currently a Principal Investigator of the EPSRC funded project on Active Quasi-optics for Power THz Science. He is a co-inventor of five patents on feed systems for satellite communications.

Dr. Dubrovka is a Reviewer of several world-leading conferences and journals on antennas and microwave devices including IEEE TAP/MTT, IET MAP, *Electronic Letters*, EuCAP, etc. He is a member of the IET.